Journal of Materials Chemistry A

PAPER

View Article Online
View Journal | View Issue

Cite this: J. Mater. Chem. A, 2014, 2, 13854

Branch-structured Bi_2S_3–CNT hybrids with improved lithium storage capability†

Yang Zhao,‡[a] Tingting Liu,‡[a] Hui Xia,[b] Ling Zhang,[a] Jiaxing Jiang,[c] Ming Shen,[d] Jiangfeng Ni*[a] and Lijun Gao[a]

Received 30th May 2014
Accepted 23rd June 2014

DOI: 10.1039/c4ta02717e

www.rsc.org/MaterialsA

Bismuth sulfide (Bi_2S_3) is a promising Li-storage material due to its high gravimetric and volumetric capacities. However, this intrinsic merit has often been compromised by the poor cycle and rate capability due to the lack of structural integrity upon the Li insertion/extraction process. Here, we engineer a branch-structured bismuth sulfide–carbon nanotube (CNT) hybrid by growing Bi_2S_3 nanorods onto CNTs to mitigate this issue. The hierarchical Bi_2S_3–CNT hybrids possess high surface areas, rich porosity for electrolyte infiltration, and direct electron transport pathways, and can be employed as efficient electrode materials for Li storage. These electrochemical results show that the Bi_2S_3–CNT hybrid exhibits a high reversible capacity (671 mA h g^{-1} at 120 mA g^{-1}), stable cycling retention (534 mA h g^{-1} after 90 cycles), and remarkable rate capability (399 mA h g^{-1} at 3000 mA g^{-1}), notably outperforming other reported Bi_2S_3 materials. Such superb Li storage capabilities suggest that the Bi_2S_3–CNT branches could be potential electrodes for rechargeable batteries.

1 Introduction

Increasing concerns on depletion of fossil fuels and environmental pollution lead to a desire to use renewable energy such as solar and wind energies. However, the intermittent characteristics of such renewable energies present tremendous challenges, and thus demand elaborate integration with energy storage systems (ESSs).[1] Amongst currently available ESSs, the Li-ion battery is surely one of the most promising systems due to its high energy density, great flexibility, and environmental benignity.[2] Despite ongoing advancement, current Li-ion batteries are limited by the performance challenges of electrode materials in terms of low energy and power density. To meet the ever-growing demand for higher energy, it is essential to utilize high-capacity anode materials such as metal oxides and sulfides to replace graphite. Through distinct conversion and/or alloying mechanisms, these compounds could afford a capacity up to 600–1000 mA h g^{-1},[3–6] substantially beyond that of their graphite counterpart (372 mA h g^{-1}).[7]

Among the chalcogenides for Li storage, bismuth sulfides (Bi_2S_3) have attracted growing attention in recent years. Featuring a direct band gap of 1.3 eV, Bi_2S_3 has been well explored as an important type of semiconductor for versatile applications such as optics,[8] magnetics,[9] biology[10] and energy generation.[11,12] Specifically, Bi_2S_3 is regarded as an ideal host for hydrogen[13,14] and lithium storage,[15–18] owing to its unique laminar structure. In contrast to many other metal chalcogenides such as Fe_3O_4,[19] MoO_3,[20,21] and MoS_2 (ref. 22) that store Li mainly through a conversion reaction, Bi_2S_3 storing Li involves successive conversion and alloying processes with a maximum Li uptake of 6.25 Li per unit formula of Bi_2S_3. This leads to theoretical capacities of 625 mA h g^{-1} by mass or ~4250 mA h cm^{-3} by volume, which are 70% or 420% greater than those of current graphite, respectively.

However, Bi_2S_3 materials often suffer from unstable performance associated with the poor conductivity and structural integrity induced by huge volume expansion upon Li cycling, which severely compromises their potential in advanced Li-ion batteries. For instance, Ma *et al.*[16] reported that uniform Bi_2S_3 fabrics could deliver 1083 mA h g^{-1} initially but only retained 366 mA h g^{-1} after 10 cycles. Jin *et al.* also demonstrated that flower-like Bi_2S_3 retained a low capacity of 169 mA h g^{-1} after 30 cycles.[18] To address this challenge, researchers engineered many Bi_2S_3 composites. Jung *et al.* fabricated fine Bi_2S_3–carbon nanocomposites that retained ~490 mA h g^{-1} for Bi_2S_3 alone over 100 cycles.[15] However, the excessive carbon (30 wt%) in the composite presents a significant challenge for real application.

[a]School of Energy, College of Physics, Optoelectronics and Energy & Collaborative Innovation Center of Suzhou Nano Science and Technology, Soochow University, Suzhou 215006, China. E-mail: jeffni@suda.edu.cn; Fax: +86-512-67875503; Tel: +86-512-67875503

[b]Herbert Gleiter Institute of Nanoscience, Nanjing University of Science and Technology, Nanjing 210094, China

[c]Wuxi Jiefu Electroacoustic Co., Ltd, Wuxi, Jiangsu 214192, China

[d]Huasheng Chemical Corporation, Zhangjiagang, Jiangsu 215635, China

† Electronic supplementary information (ESI) available: SEM and TEM images and electrochemical performance of free Bi_2S_3 microspheres. See DOI: 10.1039/c4ta02717e

‡ These authors contributed equally to this work.

Zhang *et al.* demonstrated that the Bi_2S_3–RGO (reduced graphene oxide) achieved a capacity of 400.5 mA h g^{-1} over 50 cycles.[23] Previously, we reported that the carbon coated Bi_2S_3 nanomeshes demonstrated 472 mA h g^{-1} at 120 mA g^{-1} over 50 cycles, and retained 301 mA h g^{-1} at 600 mA g^{-1} over 40 cycles.[24] However, both the cycling and rate capability still need further improvement to meet the stringent performance requirement for practical applications.

In this work, we demonstrate the synthesis and Li storage capability of a bismuth sulfide–carbon nanotube (CNT) branched hybrid (denoted as Bi_2S_3–CNT). This hybrid is fabricated *via* a facile sonochemical approach followed by crystallization in dimethyl formamide (DMF). The hierarchical Bi_2S_3–CNT hybrid exhibits unique structural features such as high surface areas, rich porosity, intrinsic flexibility, and direct electron transport pathways. These features ensure rapid electron and ion movement and stable structural integrity upon Li cycling (Fig. 1).[25] As a consequence, the Bi_2S_3–CNT hybrids display enhanced Li-storage performance outperforming previously reported Bi_2S_3 materials.

2 Experimental

2.1 Sample preparation

The synthesis of the Bi_2S_3–CNT hybrid involves sonochemical hydrolysis of $Bi(NO_3)_3$ in the presence of thioacetamide (TAA) and CNTs. In a typical operation, 20 mg HNO_3-treated CNTs (Shenzhen Nanoport, 20–30 nm in diameter) were dispersed in 40 mL aqueous solution containing 75 mg TAA (Sinopharm Chemicals) by sonication. To this mixture 5 mL of 0.4 M HNO_3 solution containing 0.243 g $Bi(NO_3)_3 \cdot 5H_2O$ was slowly added, and the suspension was further agitated for 1 hour. The resultant precipitation was then dispersed in 20 mL DMF and solvothermally treated at 150 °C for 2 hours. A free Bi_2S_3 sample was also prepared *via* the identical route without CNTs.

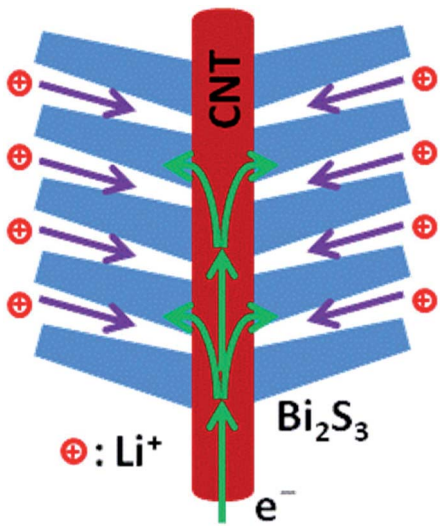

Fig. 1 Schematic illustration of electron and ion transport in the Bi_2S_3–CNT branched structure.

2.2 Characterization

The Bi_2S_3–CNT samples were characterized by X-ray diffraction (XRD, Rigaku Dmax-2400 automatic diffractometer), scanning electron microscopy (SEM, Hitachi S-4800), transmission electron microscopy (TEM, FEI Tecnai G2 T20), Fourier transform infrared spectroscopy (FTIR, Bruker Tensor 27), thermogravimetry and differential thermal analysis (TG-DTA, Seko TG/DTA-7300), and nitrogen adsorption and desorption (Micromeritics Tristar 3020).

The electrochemical Li storage performance of the Bi_2S_3–CNT was evaluated by coin-type 2032 cells using composite electrodes consisting of 70% active material, 20% Super-P-Li carbon black, and 10% polyvinylidene fluoride binder. The typical loading of the active material was 1.0–1.5 mg cm^{-2}. Cells were assembled in an Ar-filled glove box (MBraun) with both water and oxygen concentrations below 1 ppm. The counter and reference electrode are Li metal foil, the electrolyte is 1 M $LiPF_6$ solution in ethylene carbonate and dimethyl carbonate (1 : 1 by volume), and the separator is the Celgard 2320 membrane. Cyclic voltammetry (CV) and electrochemical impedance spectroscopy (EIS) were performed on a Zennium electrochemical workstation (Zahner). Galvanostatic charge and discharge tests were performed on a LAND battery test system (Jinnuo) at room temperature.

3 Results and discussion

Morphologies of the Bi_2S_3–CNT hybrid were observed by SEM and TEM, and the images are illustrated in Fig. 2. The Bi_2S_3–CNT hybrid after sonochemical reaction shows a branched structure, where the CNT backbones are decorated with numerous Bi_2S_3 nanorods (Fig. 2a). The Bi_2S_3 branches are uniform and pretty dense, as clearly shown by the TEM image (Fig. 2c). A high-resolution TEM image of Bi_2S_3 nanorods shown in Fig. 2d reveals clear lattice fringe spacings of 0.51 and 0.40 nm, corresponding to (120) and (001) facets of orthorhombic Bi_2S_3, respectively. The (001) plane is perpendicular to the elongation direction of the nanorod, suggesting that each rod is grown along the [010] direction.[13,24] However, at this stage, the Bi_2S_3 is still in poorly crystalline state and shows certain structure disorder, as pointed out by the circles in Fig. 2d. Additionally, the lattice fringe of 0.34 nm that corresponds to (002) graphene planes confirms the presence of the CNT backbone.

After solvothermal reaction in DMF, the branched structure is well preserved (Fig. 2b). Nonetheless, the density of Bi_2S_3 nanorods is slightly reduced (Fig. 2e and f), suggesting that some Bi_2S_3 rods may be detached from CNTs in DMF. It is noted that the use of aprotic solvents is critical to maintaining the branched structure, otherwise most Bi_2S_3 rods will detach CNTs if protic solvents such as water or ethanol are employed. The Bi_2S_3 nanorods are 5–10 nm in width and 30–80 nm in length, and their growth direction is roughly perpendicular to the side surfaces of CNTs to minimize the lattice mismatch at heterojunction interfaces.[26] The high-resolution TEM image confirms that the crystallinity of Bi_2S_3 rods is much improved after the

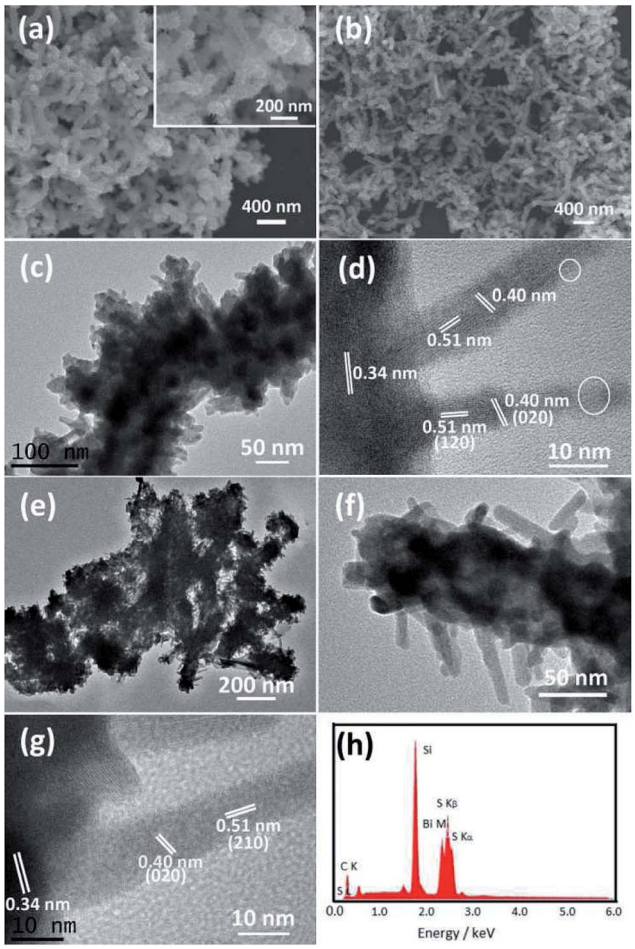

Fig. 2 SEM images of Bi_2S_3–CNT before (a) and after (b) solvothermal treatment. TEM images of Bi_2S_3–CNT before (c and d) and after (e–g) solvothermal treatment. Poorly crystalline areas of Bi_2S_3 are highlighted by circles in (d). (h) EDS of Bi_2S_3–CNT.

DMF solvothermal process (Fig. 2g). In the absence of CNTs, the obtained Bi_2S_3 sample exhibits a spherical morphology with a particle size of about 400 nm (Fig. S1 in the ESI†). The microsphere is actually composed of numerous Bi_2S_3 nanorods, consistent with Zhang's report.[27] Energy dispersive spectroscopy (EDS) shown in Fig. 1h reveals that the Bi_2S_3–CNT hybrid is composed of Bi, S, and C elements.

The structure of the Bi_2S_3–CNT was identified by XRD, as shown in Fig. 3a. The diffraction peaks in the pattern can be indexed to an orthorhombic Bi_2S_3 phase (PDF#17-0320),[13] while the (002) peak of CNTs is barely visible, possibly being masked by the surface Bi_2S_3 phase. The structure of the Bi_2S_3–CNT was further characterized by FTIR spectroscopy (Fig. 3b). The bands at 1713 and 1633 cm^{-1} are due to C=O and C=C stretching modes, respectively. The peak at 1385 cm^{-1} is assigned to C–OH stretching vibrations, while the peaks in the range of 1124–1025 cm^{-1} are due to C–O vibrations.[28] Besides these bands associated with CNTs, additional bands at 620 and 517 cm^{-1} might be attributed to C–S and O–Bi, respectively, confirming the anchoring of Bi and S species onto CNTs. The band shift of C=O from 1728 to 1713 cm^{-1} also suggests possible charge transfer between functional CNT and Bi_2S_3.

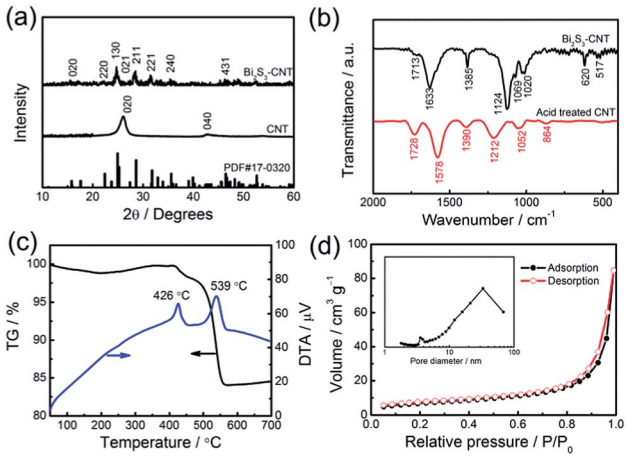

Fig. 3 (a) XRD patterns and (b) FTIR of Bi_2S_3–CNT and acid treated CNTs. (c) TG-DTA of Bi_2S_3–CNT in air. (d) N_2 adsorption and desorption isotherms and pore size distribution (inset) of Bi_2S_3–CNT.

Fig. 3c displays the TG-DTA profile of the Bi_2S_3–CNT hybrid in air. The mass loss of 1.0 wt% below 150 °C is due to dissipation of adsorbed water. The variation between 300 and 480 °C may be attributed to oxidation of Bi_2S_3, when the sulfur species may be lost as SO_2 gas or deposited as SO_4^{2-} species. The following loss of 13.7 wt% can be ascribed to burning out of CNTs.[24] Therefore, the loading of Bi_2S_3 in the hybrid is calculated to be 86.3 wt%. Despite a heavy loading of Bi_2S_3, the branched hybrid shows rich porous characteristics. Fig. 3d displays N_2 adsorption and desorption isotherms of the Bi_2S_3–CNT. The surface area of the Bi_2S_3–CNT is estimated to be 24.7 $m^2\ g^{-1}$ using the Brunauer–Emmett–Teller method, while the Barrrett–Joyner–Halenda pore volume derived from the desorption part of the isotherm is 0.13 $cm^3\ g^{-1}$. The peaks of the pore size are located at 3.6 and 33 nm, suggesting that most pores are mesopores.

The Li storage performance of the Bi_2S_3–CNT was electrochemically evaluated by CV and galvanostatic tests. Fig. 4a shows the CV profiles of the Bi_2S_3–CNT upon initial three cycles at 0.1 mV s^{-1}, which reveal a high and stable reversibility of the hybrid towards the Li reaction. The cathodic peaks at 1.79 and 1.70 V are due to the conversion reaction, where Bi_2S_3 is reduced to metallic Bi and Li_2S. The peaks at 0.70 and 0.59 V may be ascribed to the alloying process, where LiBi and Li_3Bi are formed sequentially. Compared with previous Bi_2S_3 nanomaterials, the Bi_2S_3–CNT hybrid shows an appreciable peak shift towards higher potential, suggesting reduced polarization.[24] In the reverse process, the dealloying of Li_3Bi occurs at 0.97 V, while the recovery of Bi_2S_3 at 1.83 and 2.11 V.[15] As the anodic peak of the conversion reaction is much weaker than the cathodic one, a substantial portion of Bi_2S_3 cannot be recovered and contribute to the irreversible capacity loss. An extra redox pair at 2.04/2.35 V may be associated with Li adsorption/desorption in oxygen groups of CNTs, which is generally less reversible.

Galvanostatic curves of the Bi_2S_3–CNT are presented in Fig. 4b. In the voltage window of 0.01–3.0 V, the initial

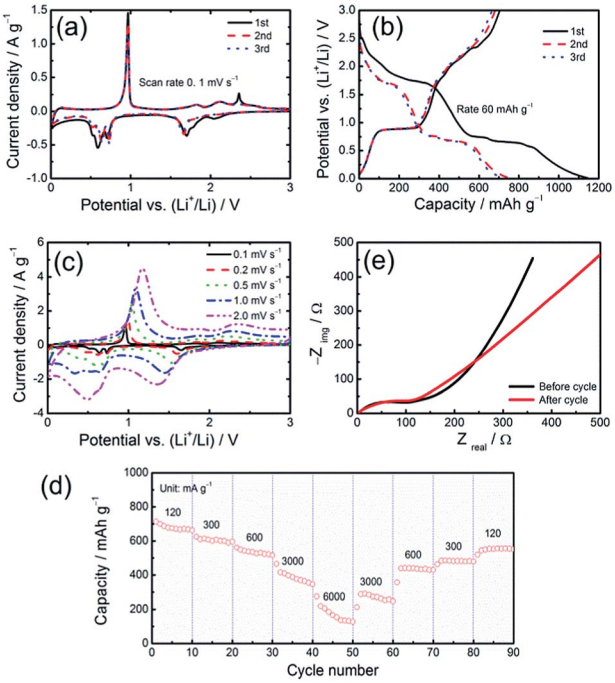

Fig. 4 (a) Initial cyclic voltammogram of Bi_2S_3–CNT at a scan rate of 0.1 mV s^{-1}. (b) Initial charge and discharge profiles of Bi_2S_3–CNT at a current rate of 60 mA g^{-1}. (c) Cyclic voltammogram of Bi_2S_3–CNT at various scan rates. (d) Cycling performance of Bi_2S_3–CNT at various current rates. (e) EIS of the Bi_2S_3–CNT electrode before and after cycling using an AC signal amplitude of 5 mV between 0.1 and 100 kHz.

capacities of the Bi_2S_3–CNT branches reach 1146 and 705 mA h g^{-1}, and the Coulombic efficiency is 61.5%. The irreversible loss may be associated with deactivation of the conversion product and formation of a solid electrolyte interphase, as frequently observed in oxide electrodes.[19,20] After two cycles, the capacity retreats to 723 and 667 mA h g^{-1} for the discharge and recharge, respectively. The actual capacity of Bi_2S_3 would be 775 and 710 mA h g^{-1} if the contribution of the CNTs (~400 mA h g^{-1}) was ruled out.[21] This capacity is evidently higher than those of free Bi_2S_3 microspheres (Fig. S2a in the ESI†) and previously reported Bi_2S_3 nanomaterials,[15,16] and even beyond the theoretical value (625 mA h g^{-1}), which could be explained by taking the rich porosity into consideration. Li storage in mesopores through adsorption/desorption is a quite common phenomenon and has been frequently reported.[29]

Besides such a high capacity delivery, the Bi_2S_3–CNT branches exhibit a remarkable rate behavior. The CV presented in Fig. 3c indicates that the Bi_2S_3–CNT can sustain rapid potential sweep. Even at a fast sweep rate of 2.0 mV s^{-1}, the Bi_2S_3–CNT retains the basic CV profile, suggesting that the electrochemical Li storage in the hybrid has barely been limited by the transport of electrons and Li ions. In addition, the galvanostatic performance further confirms that the Bi_2S_3–CNT has high-rate capability (Fig. 3d). At identical charge–discharge rates of 120, 300, 600, and 3000 mA g^{-1}, the Bi_2S_3–CNT is capable of delivering capacities of 671, 585, 527, and 399 mA h g^{-1}, respectively (taking the 2nd cycle value at each rate). The capacity delivery is also stable for 10 cycles at each rate. At an extremely high rate of 6000 mA g^{-1}, the Bi_2S_3–CNT hybrid still affords 264 mA h g^{-1}. In contrast, the free Bi_2S_3 microspheres only deliver capacities of 385 mA h g^{-1} at 600 mA g^{-1} and 250 mA h g^{-1} at 2000 mA g^{-1} (Fig. S2b in the ESI†). More importantly, when the rate is decreased, the capacity of the Bi_2S_3–CNT increases accordingly, and a high value of 534 mA h g^{-1} is recovered at the 90th cycle at 120 mA g^{-1}. These results indicate that the Bi_2S_3–CNT branches significantly outperform versatile reported Bi_2S_3 nanostructures[15,16,18,24] and Bi_2S_3–CNT[27] and Bi_2S_3–RGO[23] nanocomposites. It is also worth noting that the Li storage performance of such hybrids is comparable or even superior to some well-known sulfide composites such as SnS_2–CNT[30] and MoS_2–CNT,[31] suggesting the great potential of such branched materials.

Fig. 4e compares the EIS of the Bi_2S_3–CNT electrodes before and after 90 cycles. Both spectra are composed of two semicircles in the high and middle frequencies, and a spike in the low frequency. The interception at the Z_{real} axis refers to R_s including solution resistance and contact resistance. The high- and middle-frequency semicircles reflect the interphase resistance (R_f) and charge transfer resistance (R_{ct}), respectively.[32,33] It is clearly seen that the Bi_2S_3–CNT electrodes exhibit little variation in the spectroscopy profile after 90 cycles, implying a marked stability. This stability ensures more active material particles participating in the Li storage process, resulting in a higher level of capacity.[21]

Such an excellent Li storage capability can be correlated with the unique branched structure of the Bi_2S_3–CNT, in which the fine Bi_2S_3 branches tightly anchored on the CNT backbone. The Bi_2S_3 nanorods, 5–10 nm in width and 30–80 nm in length, drastically reduce the diffusion length of electrons and Li ions and ensure their rapid transport.[20,34] The CNT backbone serves as a flexible and express path for rapid charge transfer and thus lowers the electrode reaction resistance.[35,36] In addition, the CNT could efficiently hold cracked Bi_2S_3 particles during Li cycling and thus minimize their break of electrical contacts with the current collector. Similar phenomena have also been reported for graphene supported nanomaterials.[37,38] Moreover, the branched structure allows free penetration of the electrolyte into the bottom of Bi_2S_3 rods and thus avoids depletion of Li ions. Furthermore, the Bi_2S_3–CNT branches are intrinsically flexible, which can efficiently reduce mechanical stress and strain of the electrode upon lithiation and delithiation, thereby warranting maximum electrode stability. As a consequence, the Bi_2S_3–CNT branches exhibit a robust and stable electrochemical behavior towards Li storage.

4 Conclusions

A branch-structured Bi_2S_3–CNT hybrid was readily prepared by a facile sonochemical approach followed by solvothermal crystallization at 150 °C for 2 h. The Bi_2S_3–CNT hybrid is composed of uniform Bi_2S_3 nanorods, 5–10 nm in width and 50–100 nm in length, growing roughly perpendicular to the flexible CNT backbone. This unique Bi_2S_3–CNT hybrid can be employed as an ideal material for electrochemical Li storage. The galvanostatic test results show that the Bi_2S_3–CNT demonstrates high

reversible capacity (671 mA h g^{-1}), robust rate capability (399 mA h g^{-1} at 3000 mA g^{-1}), and stable cyclability (534 mA h g^{-1} after 90 cycles at various rates). Therefore, this work provides a facile approach to fabricate branched structures to improve the Li storage performance of Bi_2S_3 electrodes. Due to its simplicity and efficiency, this approach is intrinsically extendable and tuneable to engineering other chalcogenide materials.

Acknowledgements

Support of this work by the Natural Science Foundation of China (51302181, 51102134), China Postdoctoral Science Foundation (2014M551647), and SRF for ROCS, SEM is acknowledged.

Notes and references

1 B. Dunn, H. Kamath and J. M. Tarascon, *Science*, 2011, **334**, 928–935.
2 B. Scrosati, J. Hassoun and Y.-K. Sun, *Energy Environ. Sci.*, 2011, **4**, 3287–3295.
3 P. Poizot, S. Laruelle, S. Grugeon, L. Dupont and J. Tarascon, *Nature*, 2000, **407**, 496–499.
4 J.-M. Tarascon and M. Armand, *Nature*, 2001, **414**, 359–367.
5 A. S. Arico, P. Bruce, B. Scrosati, J. M. Tarascon and W. Van Schalkwijk, *Nat. Mater.*, 2005, **4**, 366–377.
6 J. Cabana, L. Monconduit, D. Larcher and M. R. Palacin, *Adv. Mater.*, 2010, **22**, E170–E192.
7 C. Liu, F. Li, L.-P. Ma and H.-M. Cheng, *Adv. Mater.*, 2010, **22**, E28–E62.
8 T. Wu, X. Zhou, H. Zhang and X. Zhong, *Nano Res.*, 2010, **3**, 379–386.
9 S. Luo, F. Chai, L. Zhang, C. Wang, L. Li, X. Liu and Z. Su, *J. Mater. Chem.*, 2012, **22**, 4832–4836.
10 L. Cademartiri, F. Scotognella, P. G. O'Brien, B. V. Lotsch, J. Thomson, S. Petrov, N. P. Kherani and G. A. Ozin, *Nano Lett.*, 2009, **9**, 1482–1486.
11 A. K. Rath, M. Bernechea, L. Martinez and G. Konstantatos, *Adv. Mater.*, 2011, **23**, 3712–3717.
12 Z.-H. Ge, B.-P. Zhang and J.-F. Li, *J. Mater. Chem.*, 2012, **22**, 17589–17594.
13 L. Li, N. Sun, Y. Huang, Y. Qin, N. Zhao, J. Gao, M. Li, H. Zhou and L. Qi, *Adv. Funct. Mater.*, 2008, **18**, 1194–1201.
14 R. C. Jin, Y. B. Xu, G. H. Li, J. S. Liu and G. Chen, *Int. J. Hydrogen Energy*, 2013, **38**, 9137–9144.
15 H. Jung, C.-M. Park and H.-J. Sohn, *Electrochim. Acta*, 2011, **56**, 2135–2139.
16 J. Ma, Z. Liu, J. Lian, X. Duan, T. Kim, P. Peng, X. Liu, Q. Chen, G. Yao and W. Zheng, *CrystEngComm*, 2011, **13**, 3072–3079.
17 H. Zhou, S. Xiong, L. Wei, B. Xi, Y. Zhu and Y. Qian, *Cryst. Growth Des.*, 2009, **9**, 3862–3867.
18 R. Jin, G. Li, J. Liu and L. Yang, *Eur. J. Inorg. Chem.*, 2013, **2013**, 5400–5407.
19 J. Liu, J. Ni, Y. Zhao, H. Wang and L. Gao, *J. Mater. Chem. A*, 2013, **1**, 12879–12884.
20 G. B. Wang, J. F. Ni, H. B. Wang and L. J. Gao, *J. Mater. Chem. A*, 2013, **1**, 4112–4118.
21 J. Ni, G. Wang, J. Yang, D. Gao, J. Chen, L. Gao and Y. Li, *J. Power Sources*, 2014, **247**, 90–94.
22 K. Chang, D. Geng, X. Li, J. Yang, Y. Tang, M. Cai, R. Li and X. Sun, *Adv. Energy Mater.*, 2013, **3**, 839–844.
23 Z. Zhang, C. Zhou, L. Huang, X. Wang, Y. Qu, Y. Lai and J. Li, *Electrochim. Acta*, 2013, **114**, 88–94.
24 Y. Zhao, D. Gao, J. Ni, L. Gao, J. Yang and Y. Li, *Nano Res.*, 2014, **7**, 765–773.
25 C. Zhu, X. Xia, J. Liu, Z. Fan, D. Chao, H. Zhang and H. J. Fan, *Nano Energy*, 2014, **4**, 105–112.
26 C. Cheng and H. J. Fan, *Nano Today*, 2012, **7**, 327–343.
27 Z. Zhang, C. K. Zhou, H. Lu, M. Jia, Y. Q. Lai and J. Li, *Mater. Lett.*, 2013, **91**, 100–102.
28 B. P. Vinayan, R. Nagar, V. Raman, N. Rajalakshmi, K. S. Dhathathreyan and S. Ramaprabhu, *J. Mater. Chem.*, 2012, **22**, 9949.
29 Y. Sun, X. Hu, W. Luo, F. Xia and Y. Huang, *Adv. Funct. Mater.*, 2013, **23**, 2436–2444.
30 C. Zhai, N. Du, H. Zhang, J. Yu and D. Yang, *ACS Appl. Mater. Interfaces*, 2011, **3**, 4067–4074.
31 S. Ding, J. S. Chen and X. W. Lou, *Chem.–Eur. J.*, 2011, **17**, 13142–13145.
32 J. F. Ni, H. B. Wang, L. J. Gao and L. Lu, *Electrochim. Acta*, 2012, **70**, 349–354.
33 J. F. Ni, L. J. Gao and L. Lu, *J. Power Sources*, 2013, **221**, 35–41.
34 Y. G. Wang, H. Q. Li, P. He, E. Hosono and H. S. Zhou, *Nanoscale*, 2010, **2**, 1294–1305.
35 Y. W. Cheng, S. T. Lu, H. B. Zhang, C. V. Varanasi and J. Liu, *Nano Lett.*, 2012, **12**, 4206–4211.
36 L. W. Zhao, J. F. Ni, H. B. Wang and L. J. Gao, *RSC Adv.*, 2013, **3**, 6650–6655.
37 X.-L. Huang, R.-Z. Wang, D. Xu, Z.-L. Wang, H.-G. Wang, J.-J. Xu, Z. Wu, Q.-C. Liu, Y. Zhang and X.-B. Zhang, *Adv. Funct. Mater.*, 2013, **23**, 4345–4353.
38 J. W. Zhang, L. H. Zhuo, L. L. Zhang, C. Y. Wu, X. B. Zhang and L. M. Wang, *J. Mater. Chem.*, 2011, **21**, 6975–6980.

